Supplementary materials for "Validation of XCO_2 derived from SWIR spectra of GOSAT TANSO-FTS with aircraft measurement data"

Makoto Inoue, Isamu Morino, Osamu Uchino, Yuki Miyamoto, Yukio Yoshida, Tatsuya Yokota, Toshinobu Machida, Yousuke Sawa, Hidekazu Matsueda, Colm Sweeney, Pieter P. Tans, Arlyn E. Andrews, and Prabir K. Patra

In Sect. 4.3.2, a part of the analyses using a curve fitting method was presented. Here, we show the temporal variations and comparison results at all aircraft measurement sites (Figs. A-1 to A-14). In addition, the average and 1 standard deviation of the differences between GOSAT SWIR XCO_2 and aircraft-based XCO_2 at each aircraft site using curve fitting are listed in Tables A-1 and A-2. In the mid- and high-latitudes of Asia, North America, Europe, and Siberia, apparent seasonal amplitude of approximately 7-8 ppm was observed. In contrast, seasonal changes were obscure at Sydney over the Southern Hemisphere. In most land regions, the GOSAT SWIR XCO_2 agreed well with aircraft-based XCO_2. There were also good correlations between both data sets over several ocean regions and the correlation coefficients were 0.92 and 0.61 with significance at the 99% level over Honolulu and Manila, respectively, for the $\pm$5-degree boxes.

Thus, the curve fitting method enabled us to validate the GOSAT products over all locations.

Table A- 1: The average and 1 standard deviation (1 σ) of the differences between GOSAT XCO_2 observed over land region within ±2-degree and ±5-degree latitude/longitude boxes centered at each aircraft site and aircraft-based XCO_2 using curve fitting method.

Land		±2 deg.			±5 deg.	
site	number	average [ppm]	1σ [ppm]	number	average [ppm]	1σ [ppm]
(1) AMS	14	0.481	2.262	124	-1.564	2.084
(2) LHR	40	-0.957	2.088	155	-1.112	2.063
(3) YVR	6	0.328	4.117	166	-1.373	2.471
(4) CDG	57	-1.393	1.905	262	-1.373	2.054
(5) MXP	32	0.071	2.501	181	0.444	2.481
(6) FCO	43	-1.301	2.126	195	-2.089	2.346
(7) ICN	66	0.287	2.828	189	-0.254	2.846
(8) NRT	65	-0.461	2.259	105	-0.545	2.471
(9) HND	76	-0.897	2.408	108	-1.040	2.507
(10) NGO	25	-0.459	2.792	120	-0.339	2.442
(11) KIX	18	-0.770	2.507	103	-0.162	2.484
(12) DEL	214	-1.548	1.857	854	-2.153	1.940
(13) TPE	11	0.899	1.712	70	0.559	2.165
(14) HNL	0	-	-	0	-	-
(15) MNL	0	-	-	2	-3.968	0.641
(16) BKK	18	0.215	2.214	77	-0.798	2.391
(17) GUM	0	-	-	0	-	-
(18) SIN	0	-	-	0	-	-
(19) CGK	2	-1.147	0.565	5	-1.561	0.616
(20) SYD	83	-0.740	2.314	370	-1.448	2.067
(21) PFA	37	0.574	1.990	108	-0.653	2.322
(22) BRM	43	-0.018	2.944	286	-0.991	2.810
(23) ESP	0	-	-	84	-0.826	2.529
(24) DND	70	-2.264	1.689	402	-1.483	2.455
(25) LEF	60	-1.623	2.359	299	-1.412	2.641
(26) NHA	23	-1.602	1.431	169	-1.106	2.290
(27) WBI	44	-2.210	2.434	615	-2.246	1.954
(28) THD	80	0.147	2.282	329	-0.746	2.087
(29) BNE	132	-3.014	1.909	765	-3.095	2.295
(30) CAR	161	-3.542	1.678	766	-3.287	2.004
(31) HIL	173	-2.514	1.615	628	-2.416	1.933
(32) AAO	139	-1.122	2.002	621	-1.140	2.073
(33) CMA	45	-0.933	2.417	205	-1.410	2.322
(34) SGP	184	-2.809	1.740	835	-2.745	1.926
(35) SCA	80	-1.636	1.763	521	-1.548	1.908
(36) TGC	47	-1.491	1.639	546	-1.709	1.705
(37) RTA	0	-	-	0	-	-
(38) YKT	50	-1.962	2.303	183	-2.070	2.408
(39) SRG	52	-2.150	2.495	269	-2.752	2.633
(40) NVS	53	-1.250	2.593	323	-1.469	2.823
(41) SGM	70	0.594	2.494	106	0.384	2.575
All data	2313	-1.555	2.364	11146	-1.813	2.373

Table A- 2: The average and 1 standard deviation (1 σ) of the differences between GOSAT XCO_2 observed over ocean region within ±2-degree and ±5-degree latitude/longitude boxes centered at each aircraft site and aircraft-based XCO_2 using curve fitting method.

Ocean		±2 deg.			±5 deg.	
site	number	average [ppm]	1σ [ppm]	number	average [ppm]	1σ [ppm]
(1) AMS	0	-	-	0	-	-
(2) LHR	0	-	-	1	-1.712	-
(3) YVR	0	-	-	1	0.699	-
(4) CDG	0	-	-	0	-	-
(5) MXP	1	0.793	-	4	-0.732	1.562
(6) FCO	0	-	-	31	-4.652	2.164
(7) ICN	0	-	-	55	-1.661	3.537
(8) NRT	1	0.455	-	9	-2.952	3.051
(9) HND	1	0.414	-	10	-2.631	2.770
(10) NGO	0	-	-	19	-2.435	4.009
(11) KIX	0	-	-	35	-2.699	3.565
(12) DEL	0	-	-	0	-	-
(13) TPE	19	-0.633	2.704	38	-0.283	2.835
(14) HNL	30	-2.062	1.271	98	-1.639	1.330
(15) MNL	0	-	-	66	-1.857	1.664
(16) BKK	4	-4.054	1.868	11	-3.500	1.505
(17) GUM	1	0.834	-	44	-0.750	-1.454
(18) SIN	1	-1.503	-	4	-2.151	0.772
(19) CGK	3	-1.161	1.361	21	-2.049	1.495
(20) SYD	1	-1.578	-	54	-1.538	1.544
(21) PFA	0	-	-	0	-	-
(22) BRM	0	-	-	0	-	-
(23) ESP	1	0.901	-	1	0.901	-
(24) DND	0	-	-	0	-	-
(25) LEF	0	-	-	0	-	-
(26) NHA	1	-0.927	-	6	-2.934	1.999
(27) WBI	0	-	-	0	-	-
(28) THD	0	-	-	3	-1.172	3.231
(29) BNE	0	-	-	0	-	-
(30) CAR	0	-	-	0	-	-
(31) HIL	0	-	-	0	-	-
(32) AAO	0	-	-	0	-	-
(33) CMA	3	-2.070	1.142	24	-1.094	2.491
(34) SGP	0	-	-	0	-	-
(35) SCA	0	-	-	63	-0.959	1.959
(36) TGC	0	-	-	58	-1.501	1.379
(37) RTA	17	-1.939	1.561	45	-2.170	1.280
(38) YKT	0	-	-	0	-	-
(39) SRG	0	-	-	0	-	-
(40) NVS	0	-	-	0	-	-
(41) SGM	1	3.845	-	7	0.093	3.513
All data	85	-1.524	2.016	708	-1.729	2.349

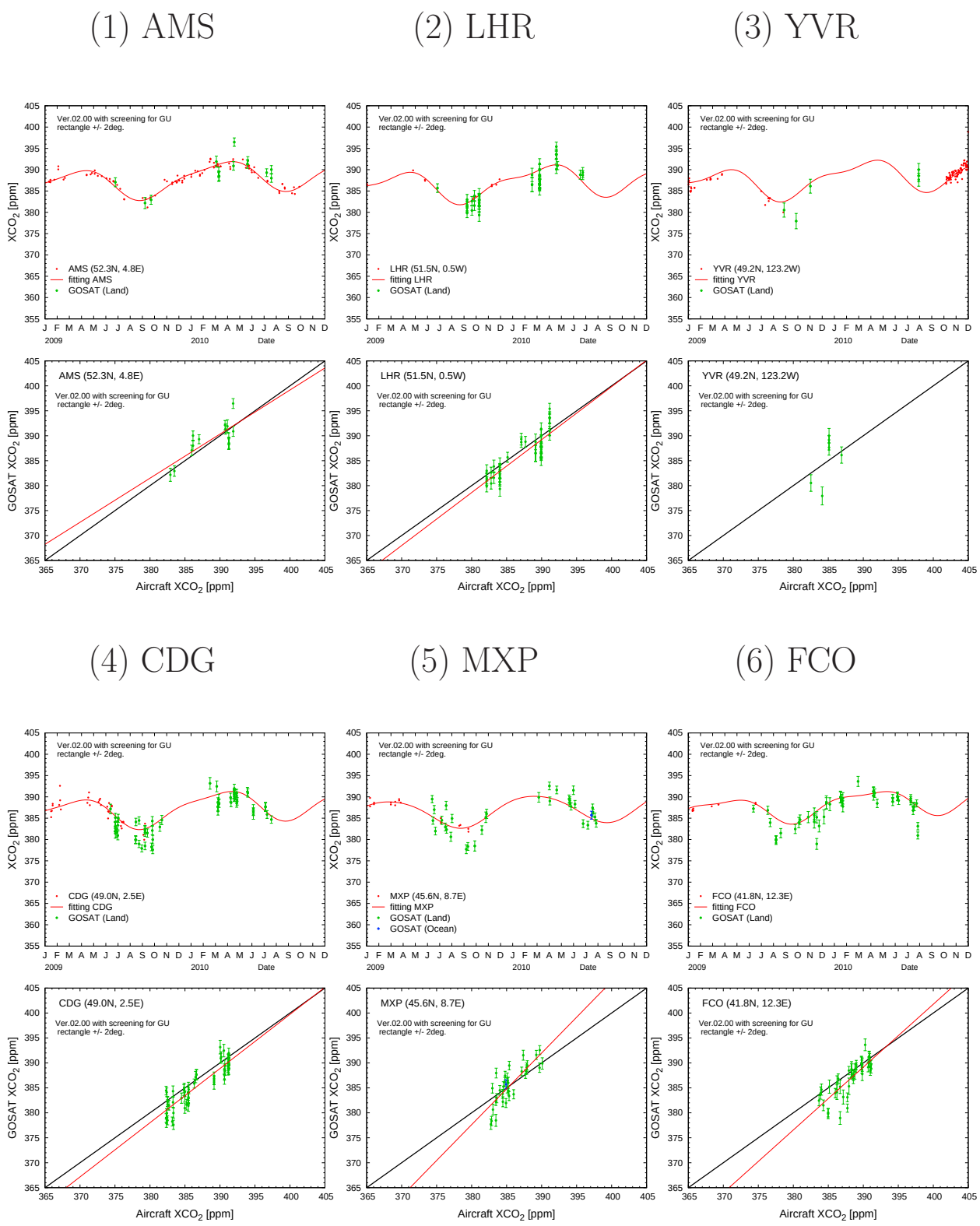

Fig. A- 1: Temporal variations of aircraft-based XCO_2 and GOSAT XCO_2 observed within ±2-degree latitude/longitude boxes centered at each aircraft site (upper panels) and their scatter diagrams (bottom panels) for (1) Amsterdam, (2) London, (3) Vancouver, (4) Paris, (5) Milan, and (6) Rome. Green and blue dots show the XCO_2 data over land and ocean regions, respectively. Red dots and lines in the upper panels indicate the aircraft-based XCO_2 and fitted curves based on their data, respectively. Red and blue lines in the bottom panels denote the regression lines with statistical significance at the 95% level over land and ocean regions, respectively. The one-to-one lines are plotted as black lines.

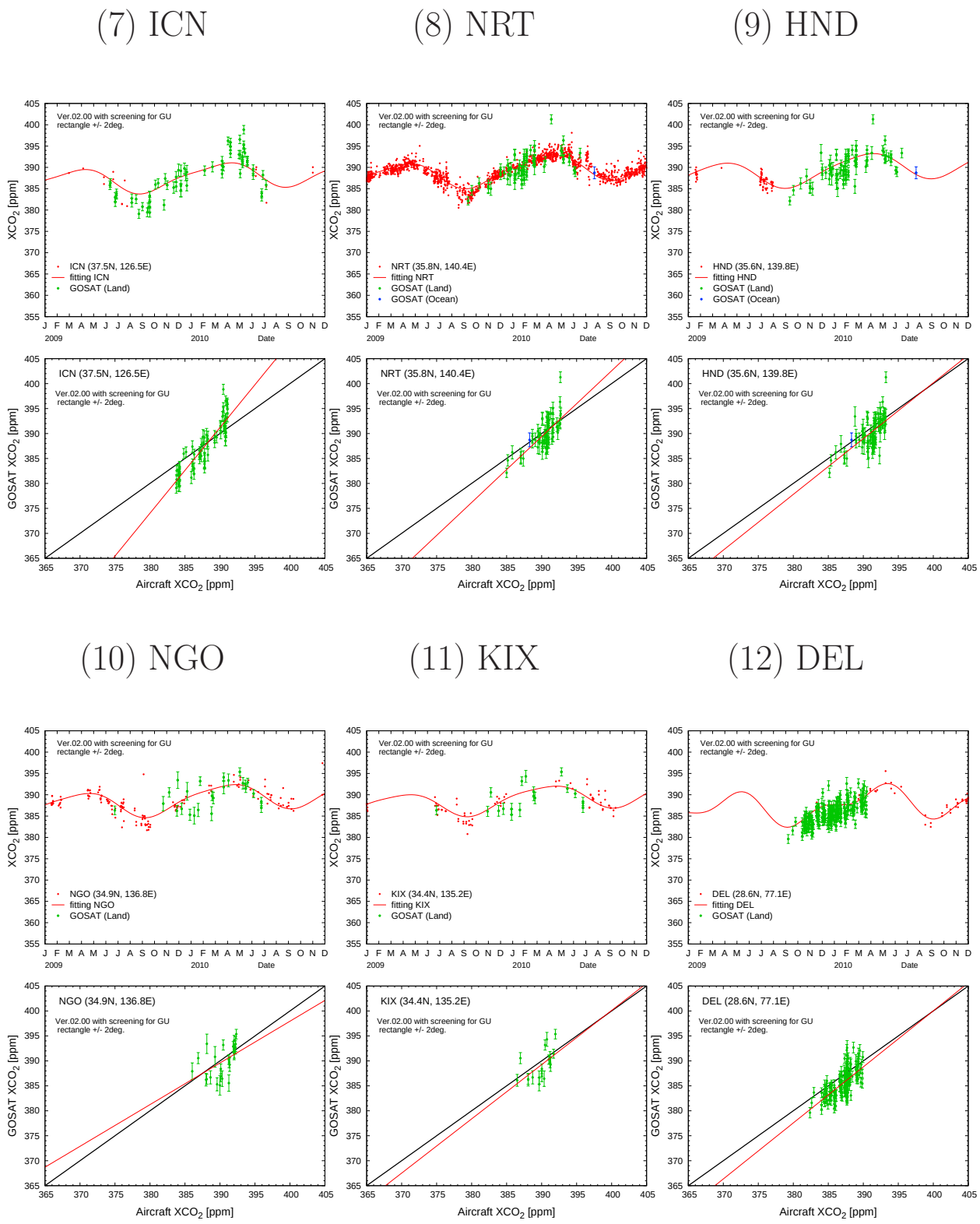

Fig. A- 2: Temporal variations of aircraft-based XCO_2 and GOSAT XCO_2 observed within ±2-degree latitude/longitude boxes centered at each aircraft site (upper panels) and their scatter diagrams (bottom panels) for (7) Incheon, (8) Narita, (9) Haneda, (10) Nagoya, (11) Kansai, and (12) Dehli. The others are the same as in Fig. A-1.

(13) TPE (14) HNL (15) MNL

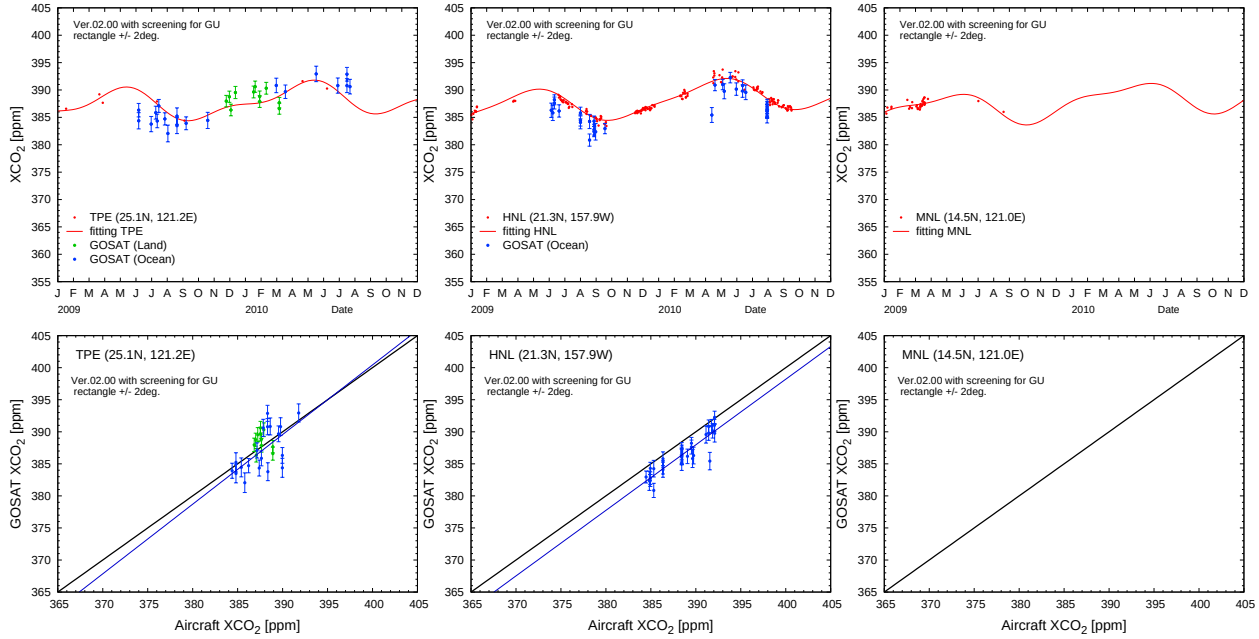

(16) BKK (17) GUM (18) SIN

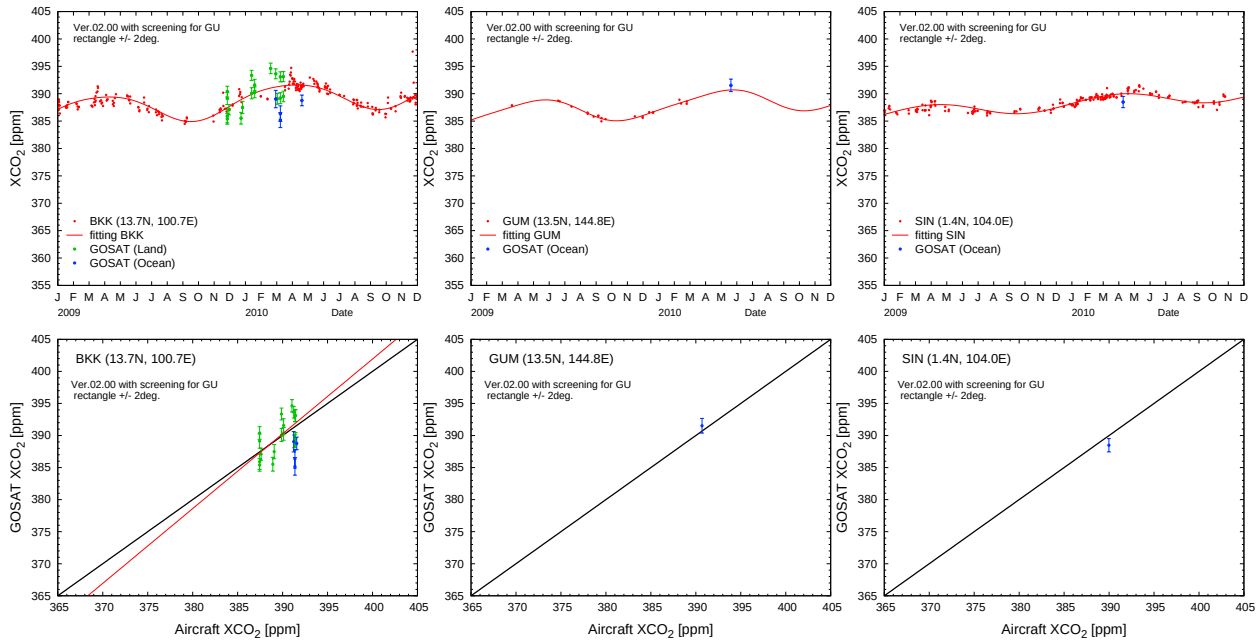

Fig. A- 3: Temporal variations of aircraft-based XCO_2 and GOSAT XCO_2 observed within ±2-degree latitude/longitude boxes centered at each aircraft site (upper panels) and their scatter diagrams (bottom panels) for (13) Taipei, (14) Honolulu, (15) Manila, (16) Bangkok, (17) Guam, and (18) Singapore. The others are the same as in Fig. A-1.

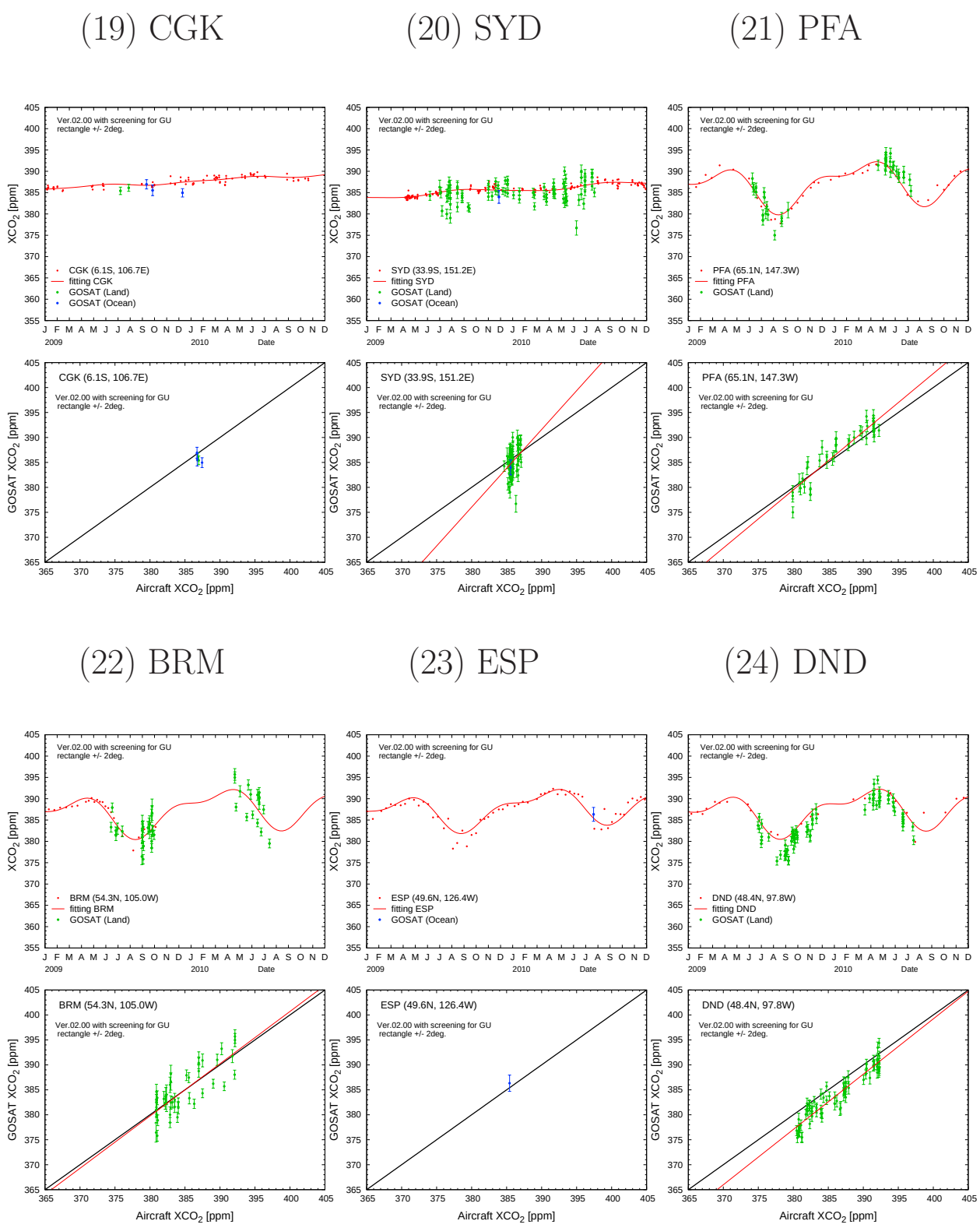

Fig. A- 4: Temporal variations of aircraft-based XCO_2 and GOSAT XCO_2 observed within ±2-degree latitude/longitude boxes centered at each aircraft site (upper panels) and their scatter diagrams (bottom panels) for (19) Jakarta, (20) Sydney, (21) Poker Flat, (22) BERMS, (23) Estevan Point, and (24) Dahlen. The others are the same as in Fig. A-1.

(25) LEF (26) NHA (27) WBI

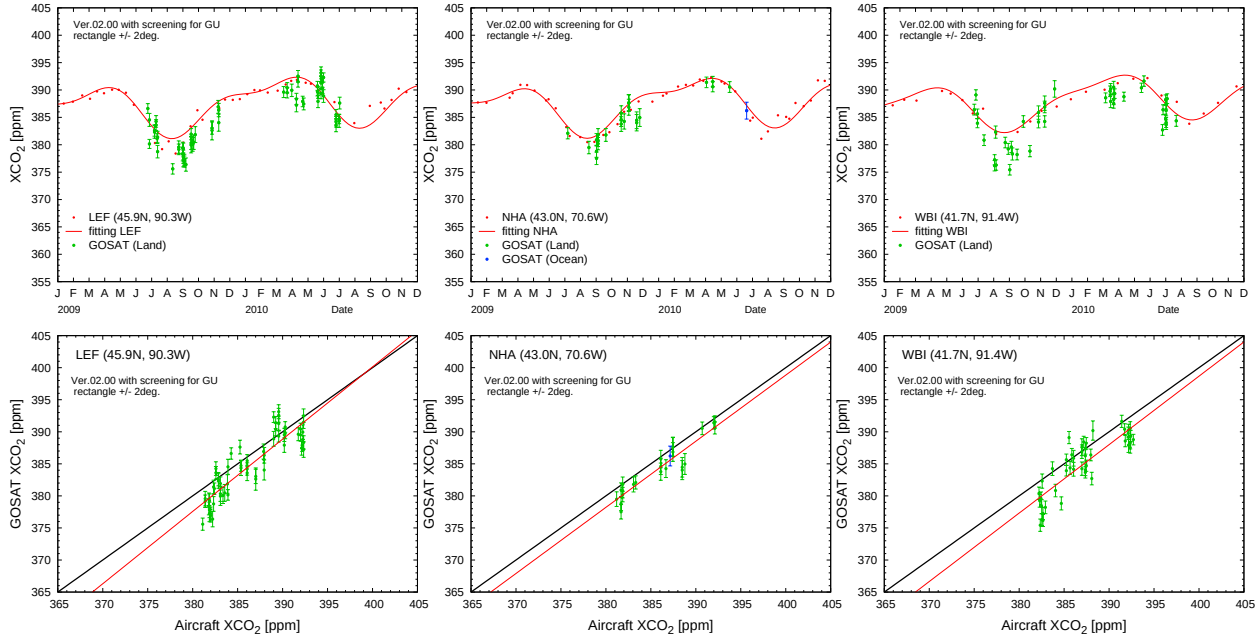

(28) THD (29) BNE (30) CAR

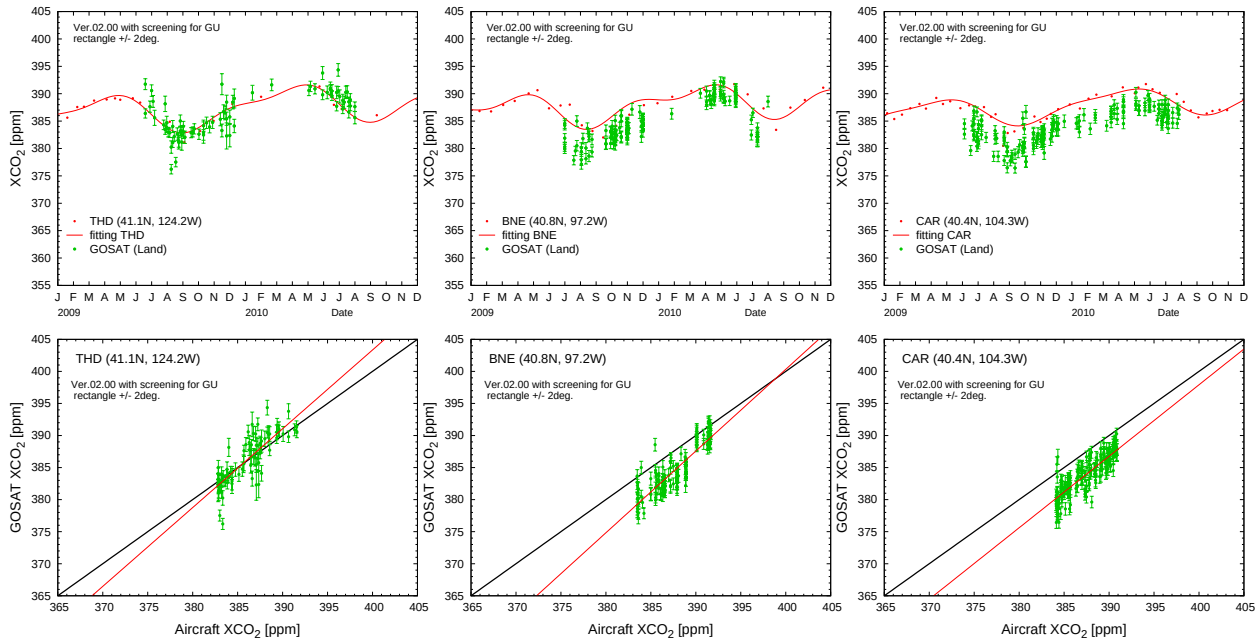

Fig. A- 5: Temporal variations of aircraft-based XCO_2 and GOSAT XCO_2 observed within ±2-degree latitude/longitude boxes centered at each aircraft site (upper panels) and their scatter diagrams (bottom panels) for (25) Park Falls, (26) Worcester, (27) West Branch, (28) Trinidad Head, (29) Beaver Crossing, and (30) Briggsdale. The others are the same as in Fig. A-1.

(31) HIL (32) AAO (33) CMA

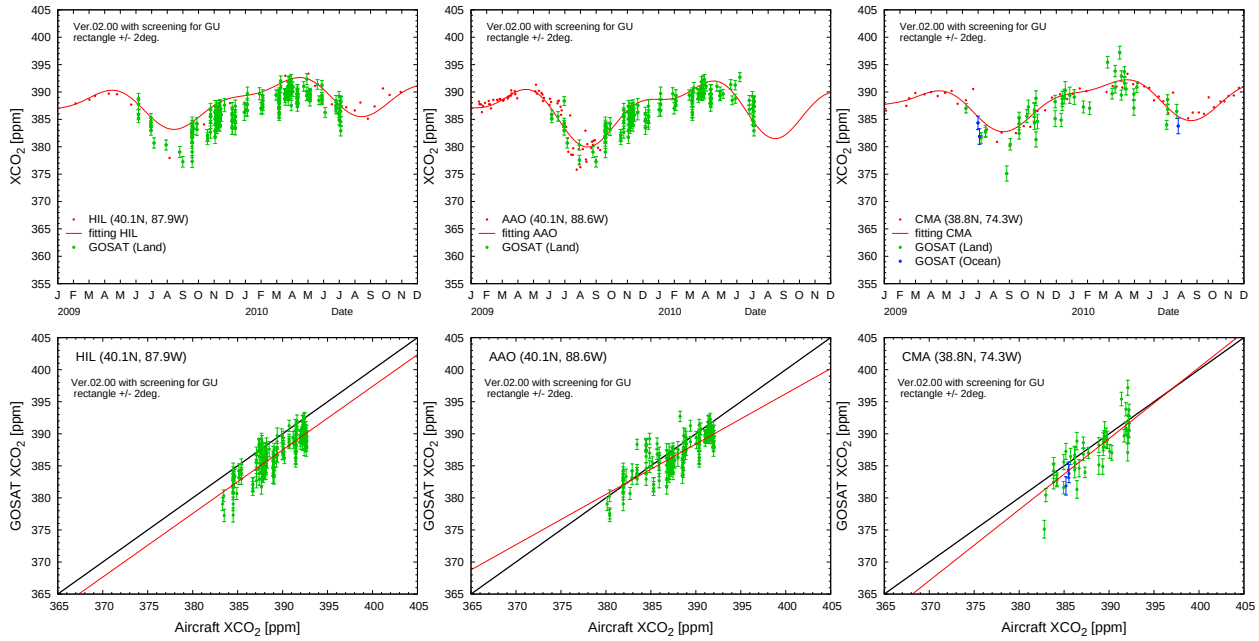

(34) SGP (35) SCA (36) TGC

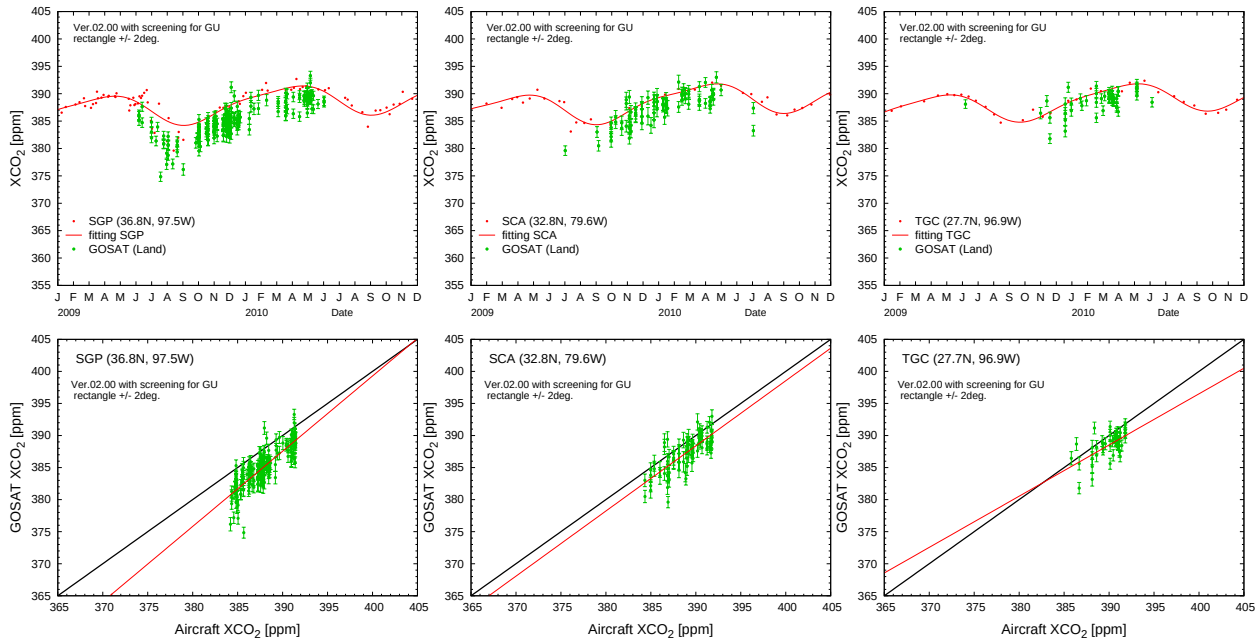

Fig. A- 6: Temporal variations of aircraft-based XCO_2 and GOSAT XCO_2 observed within ±2-degree latitude/longitude boxes centered at each aircraft site (upper panels) and their scatter diagrams (bottom panels) for (31) Homer, (32) Bondville, (33) Cape May, (34) the Southern Great Plains, (35) Charleston, and (36) Sinton. The others are the same as in Fig. A-1.

(37) RTA (38) YKT (39) SRG

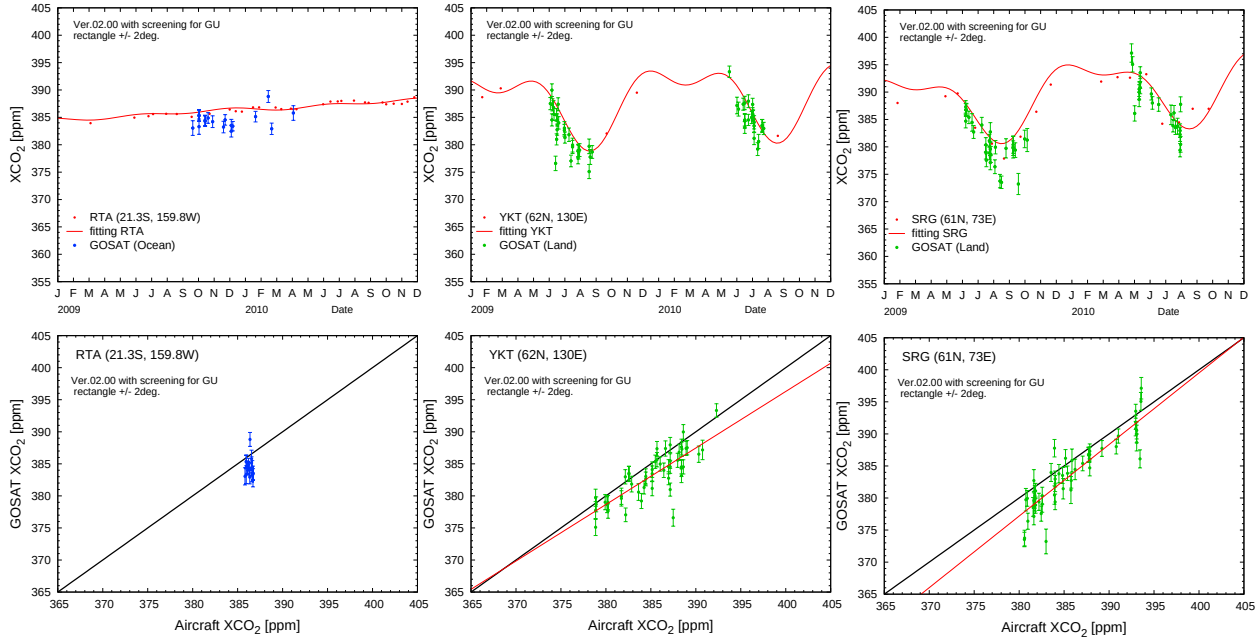

(40) NVS (41) SGM

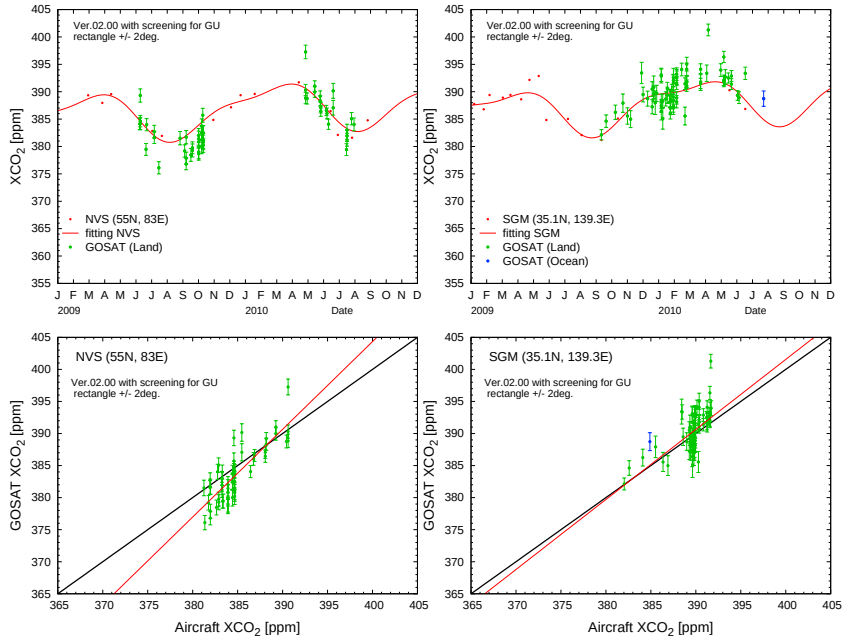

Fig. A- 7: Temporal variations of aircraft-based XCO_2 and GOSAT XCO_2 observed within ±2-degree latitude/longitude boxes centered at each aircraft site (upper panels) and their scatter diagrams (bottom panels) for (37) Rarotonga, (38) Yakutsk, (39) Surgut, (40) Novosibirsk, and (41) Sagami-bay. The others are the same as in Fig. A-1.

Fig. A- 8: Temporal variations of aircraft-based XCO_2 and GOSAT XCO_2 observed within ±5-degree latitude/longitude boxes centered at each aircraft site (upper panels) and their scatter diagrams (bottom panels) for (1) Amsterdam, (2) London, (3) Vancouver, (4) Paris, (5) Milan, and (6) Rome. The others are the same as in Fig. A-1.

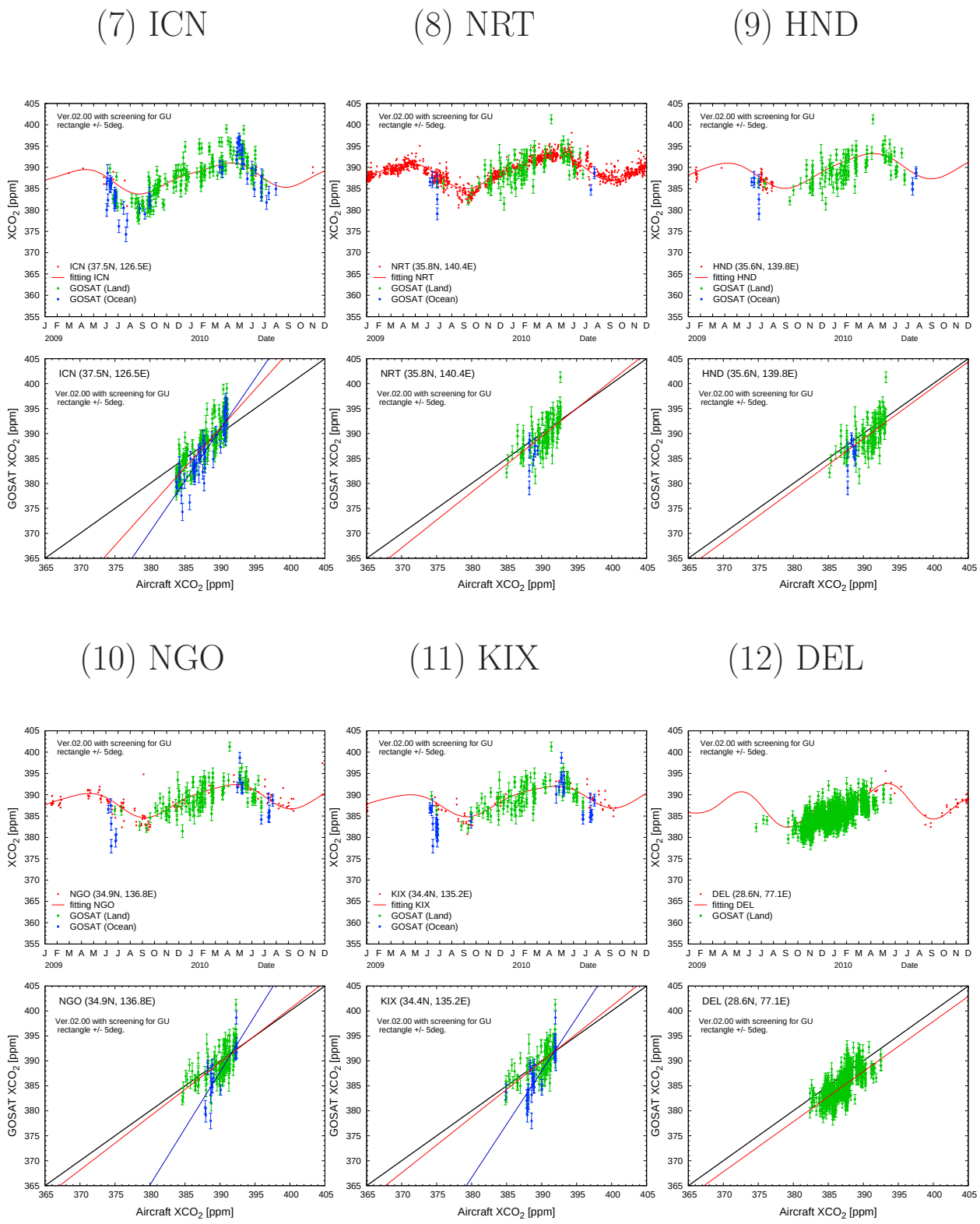

Fig. A- 9: Temporal variations of aircraft-based XCO_2 and GOSAT XCO_2 observed within ±5-degree latitude/longitude boxes centered at each aircraft site (upper panels) and their scatter diagrams (bottom panels) for (7) Incheon, (8) Narita, (9) Haneda, (10) Nagoya, (11) Kansai, and (12) Delhi. The others are the same as in Fig. A-1.

(13) TPE (14) HNL (15) MNL

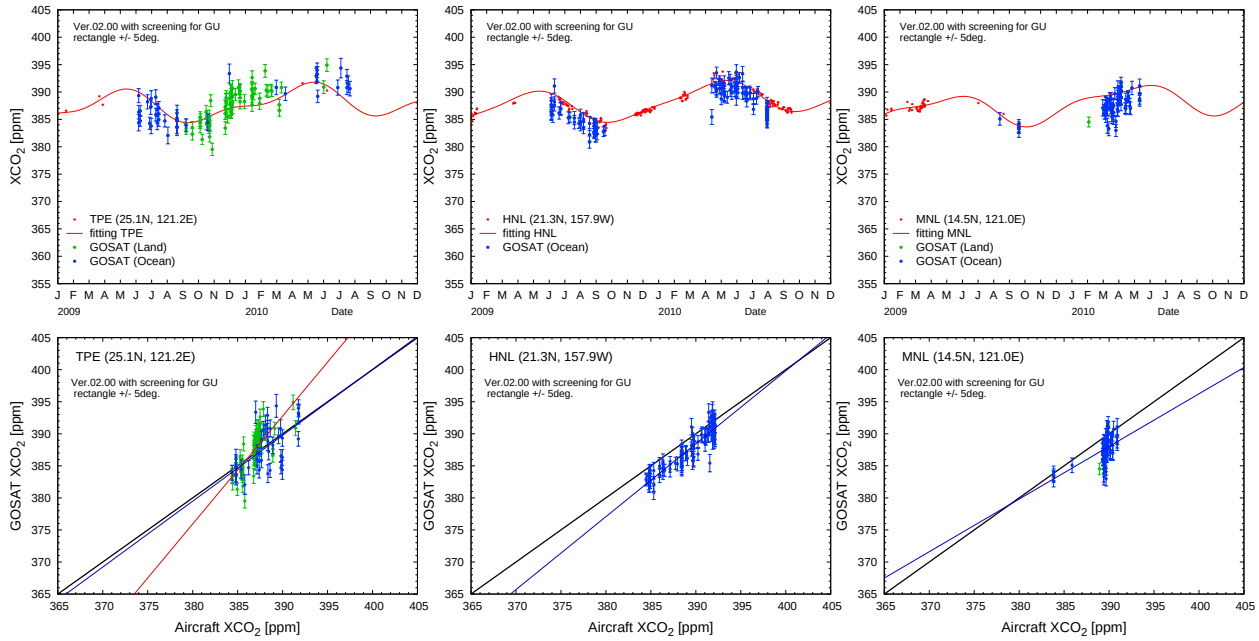

(16) BKK (17) GUM (18) SIN

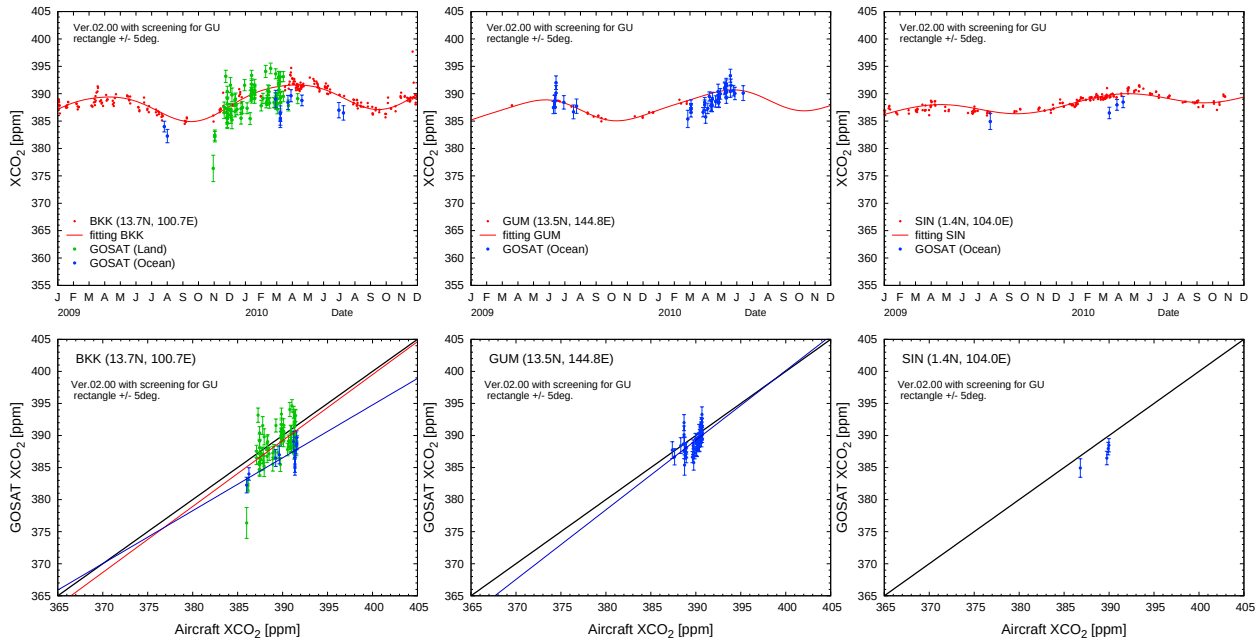

Fig. A- 10: Temporal variations of aircraft-based XCO_2 and GOSAT XCO_2 observed within ±5-degree latitude/longitude boxes centered at each aircraft site (upper panels) and their scatter diagrams (bottom panels) for (13) Taipei, (14) Honolulu, (15) Manila, (16) Bangkok, (17) Guam, and (18) Singapore. The others are the same as in Fig. A-1.

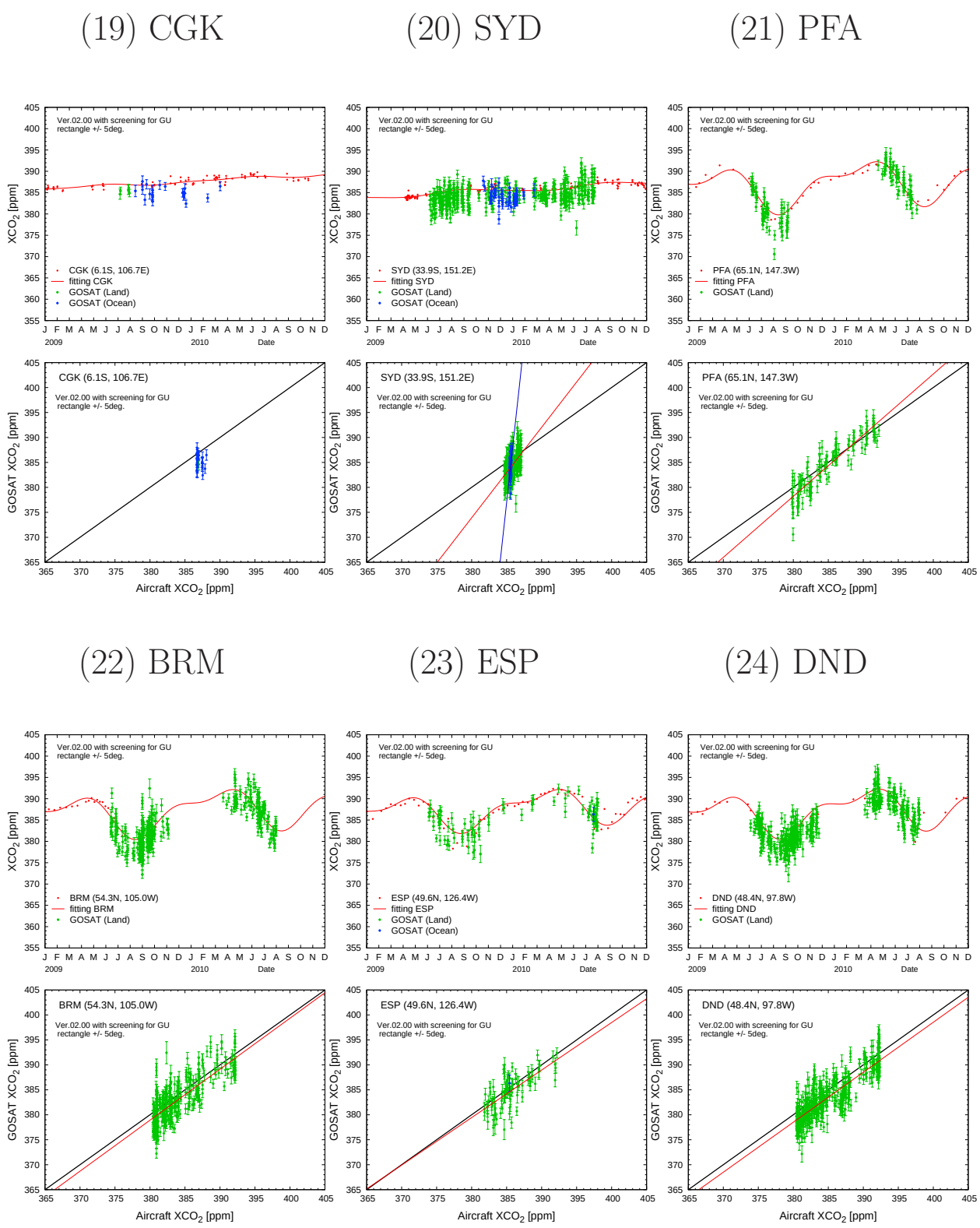

Fig. A- 11: Temporal variations of aircraft-based XCO_2 and GOSAT XCO_2 observed within ±5-degree latitude/longitude boxes centered at each aircraft site (upper panels) and their scatter diagrams (bottom panels) for (19) Jakarta, (20) Sydney, (21) Poker Flat, (22) BERMS, (23) Estevan Point, and (24) Dahlen. The others are the same as in Fig. A-1.

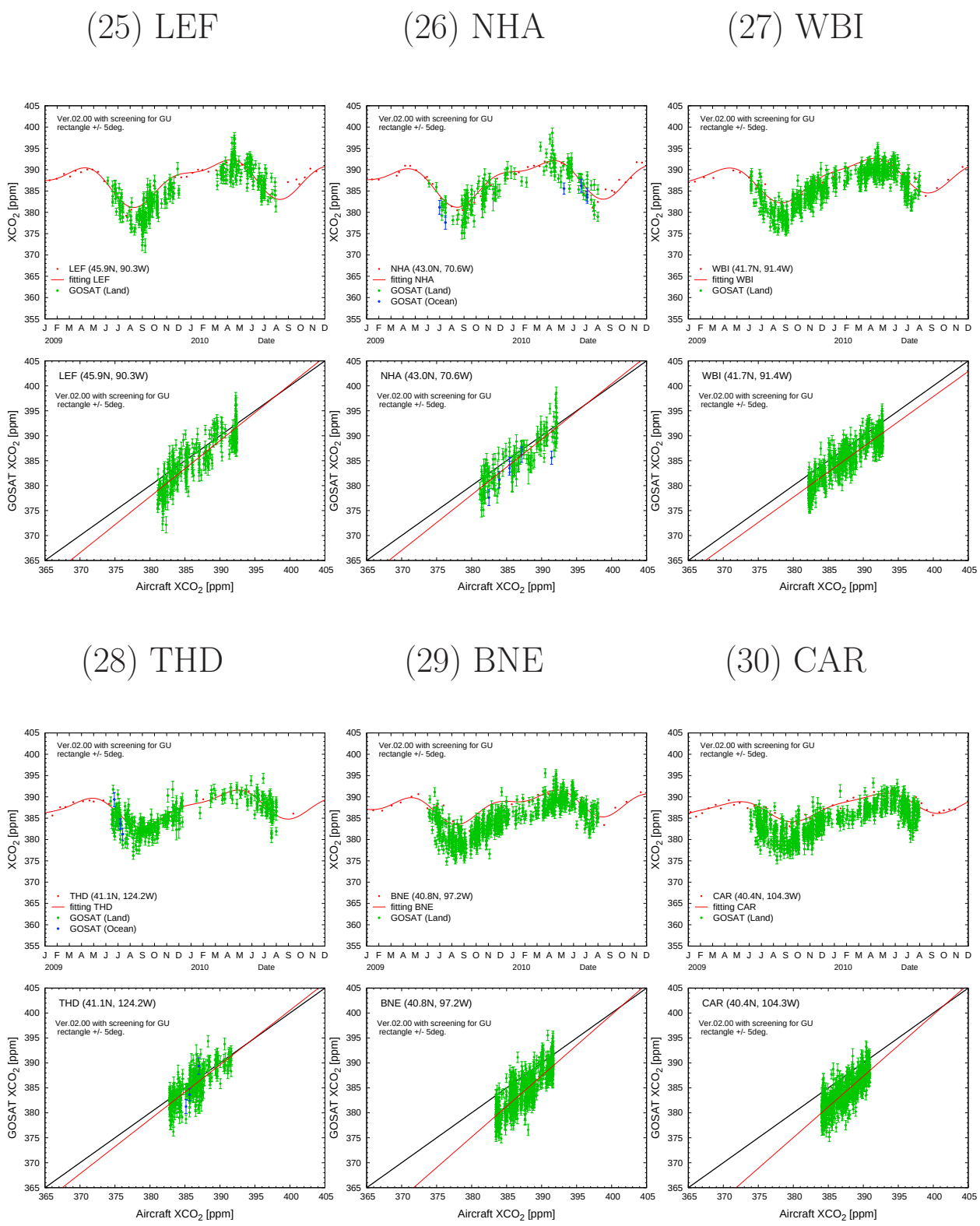

Fig. A- 12: Temporal variations of aircraft-based XCO_2 and GOSAT XCO_2 observed within ±5-degree latitude/longitude boxes centered at each aircraft site (upper panels) and their scatter diagrams (bottom panels) for (25) Park Falls, (26) Worcester, (27) West Branch, (28) Trinidad Head, (29) Beaver Crossing, and (30) Briggsdale. The others are the same as in Fig. A-1.

(31) HIL (32) AAO (33) CMA

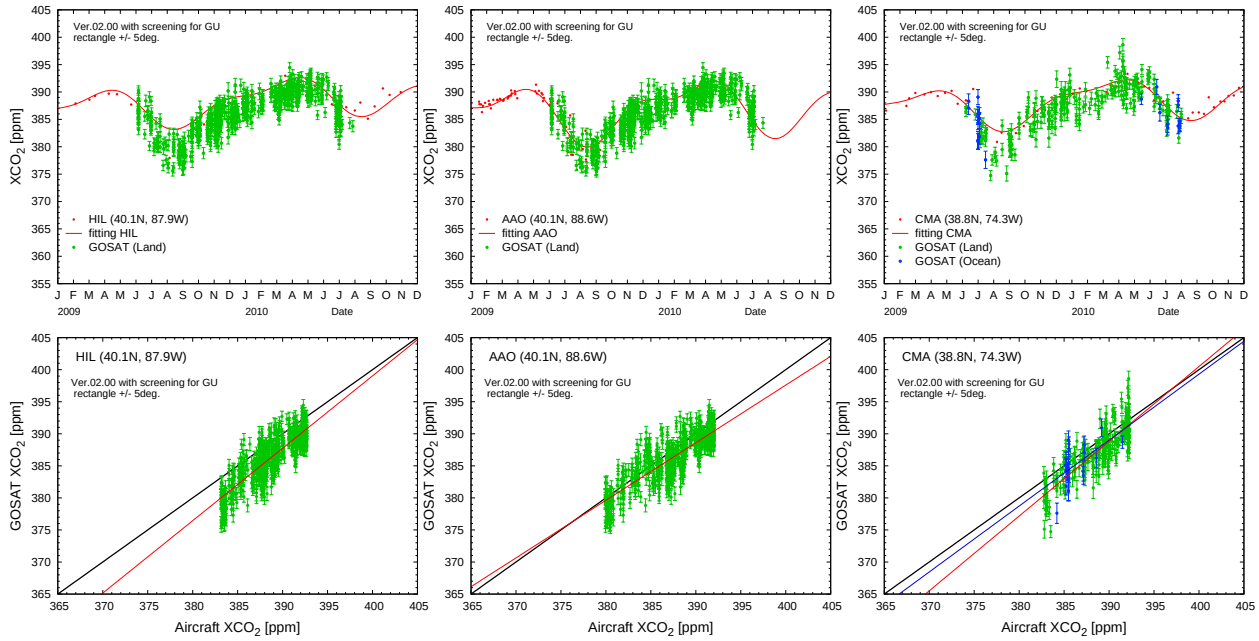

(34) SGP (35) SCA (36) TGC

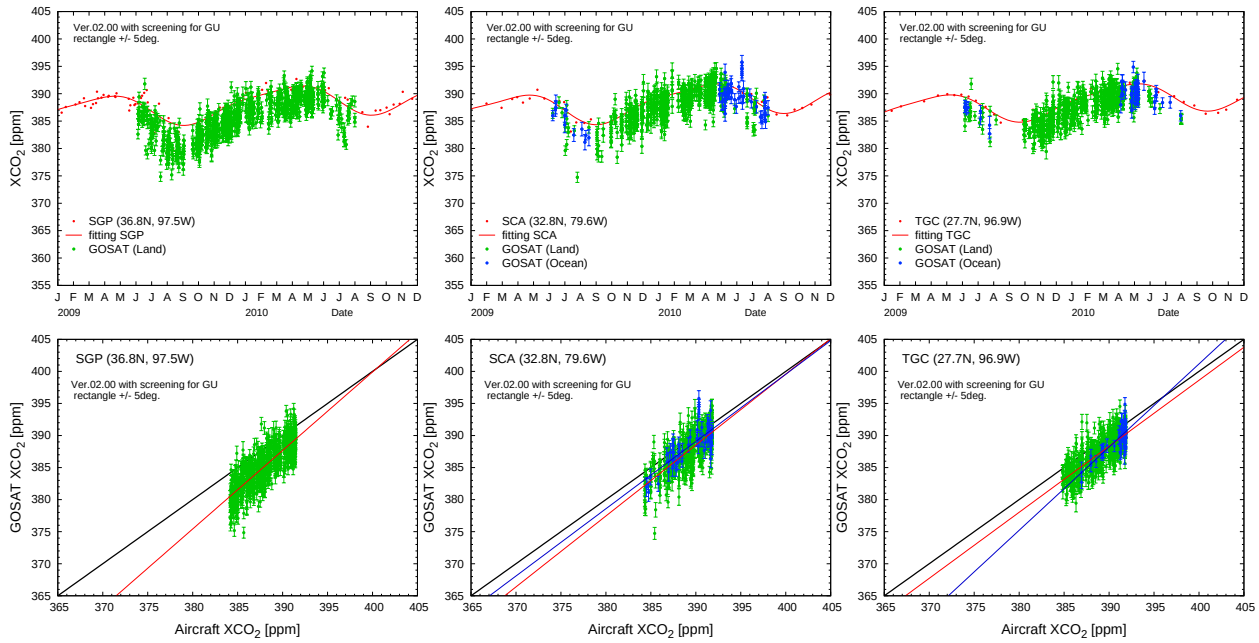

Fig. A- 13: Temporal variations of aircraft-based XCO_2 and GOSAT XCO_2 observed within ±5-degree latitude/longitude boxes centered at each aircraft site (upper panels) and their scatter diagrams (bottom panels) for (31) Homer, (32) Bondville, (33) Cape May, (34) the Southern Great Plains, (35) Charleston, and (36) Sinton. The others are the same as in Fig. A-1.

(37) RTA (38) YKT (39) SRG

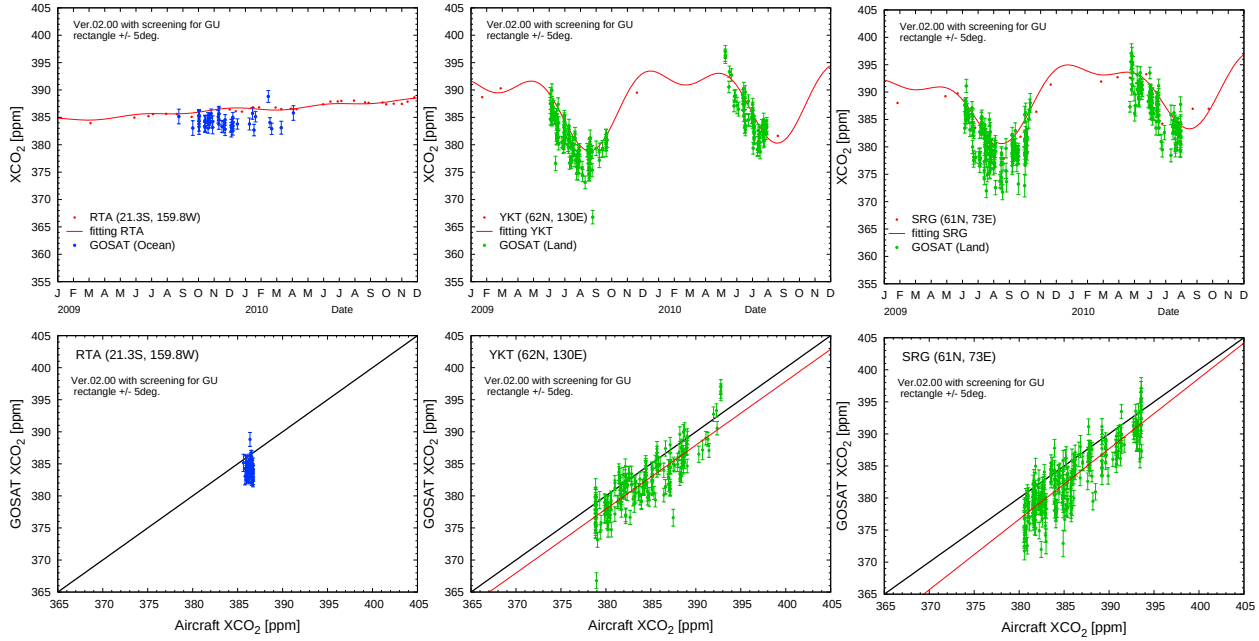

(40) NVS (41) SGM

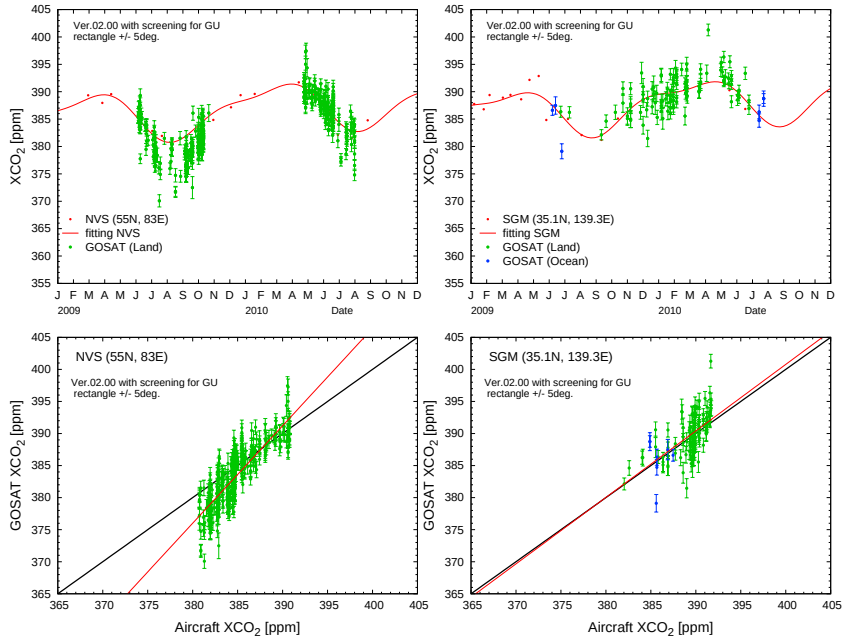

Fig. A- 14: Temporal variations of aircraft-based XCO_2 and GOSAT XCO_2 observed within ±5-degree latitude/longitude boxes centered at each aircraft site (upper panels) and their scatter diagrams (bottom panels) for (37) Rarotonga, (38) Yakutsk, (39) Surgut, (40) Novosibirsk, and (41) Sagami-bay. The others are the same as in Fig. A-1.